

Nanostructures on surfaces by ion irradiation*

Hubert Gnaser^{1,2}

¹*Department of Physics and Research Center OPTIMAS, University of Kaiserslautern, D-67663 Kaiserslautern, Germany;* ²*Institute for Surface and Thin-Film Analysis IFOS, Trippstadter Str. 120, D-67663 Kaiserslautern, Germany*

Abstract: The bombardment of the surface of a solid by energetic ions often results in pronounced surface modifications, leading to characteristic topographical features. In this report, the development of specific morphological nanostructures on surfaces under ion irradiation is discussed. The following aspects will be emphasized: (i) on an atomic scale, the generation of isolated defects such as adatoms and surface vacancies due to single-ion impacts, and their possible clustering; (ii) the transition from such individual defects toward extended morphological features on the surface and suitable scaling relations to describe them; (iii) the formation of highly periodic structures with nanoscale dimensions such as nanodots and “ripple”-like features, and the dependence of these nanostructures on various ion-irradiation parameters and substrate materials; (iv) the theoretical concepts proposed to model the observed patterns which are thought to be related to (and caused by) the interplay between ion erosion and diffusion of adatoms (vacancies), thus inducing a surface reorganization.

Keywords: ion bombardment; nanostructures; surface defects; continuum models.

INTRODUCTION

The irradiation of solid surfaces by energetic particles gives rise to a wide variety of phenomena that are correlated closely with the energy deposition processes of the incoming ions. Over a near-surface region of the solid whose extension depends primarily on the range of the incident particles, the ions transfer energy and momentum to the target atoms, displacing them from their original positions. These processes may cause the ejection of target atoms and molecule from the surface (i.e., sputtering), while displacement cascades result in an accumulation of point defects (vacancies and interstitials) or more extensive defect structures; the concurrent accumulation of the implanted species may also lead to phase changes within this zone. Several reviews have described the evolution of research in this field over the past few decades [1–10].

At the surface, ion irradiation may result in substantial morphological changes [5]. At low fluences, isolated defects such as vacancies and adatoms may be created [9]. If these defects are mobile (e.g., at elevated sample temperatures), they may annihilate or form adatom and vacancy clusters. For higher bombarding fluences, such structures may result in a coarsening of the surface; the extent of this roughening will depend again on the specimen temperature. Eventually, prolonged ion bombardment often leads to the development of a very specific surface morphology. Interestingly, these structures can have highly periodic features such as “nanodots” or “ripple”-like contours, with feature sizes in the nm-range. These self-organized nanostructures evolving due to ion irradiation on surfaces have been studied quite thoroughly in the past decade [11–14].

*Paper based on a presentation made at the International Conference on Nanomaterials and Nanotechnology (NANO-2010), Tiruchengode, India, 13–16 December 2010. Other presentations are published in this issue, pp. 1971–2113.

In this contribution, some aspects of the evolution of the surface morphology caused by ion bombardment are reviewed; the paper is organized in the following way: in the second section, the formation of surface defects such as vacancies, adatoms, and defect clusters due to single-ion impacts is described. The third section outlines the transition to more extended topographical features on surfaces, whereas the fourth section discusses ordered nanopatterns on surfaces. Theoretical concepts for the formation of such nanostructures are summarized in the fifth section. Finally, the sixth section presents examples for other nanoscaled structures created by ion irradiation. The references included cover a rather wide range of the literature available in this research field, but are not meant to be exhaustive.

FORMATION OF SURFACE DEFECTS: VACANCIES, ADATOMS, AND DEFECT CLUSTERING

Many earlier studies into the production of defects in solids due to ion irradiation concentrated primarily on effects within the bulk of the material or on the sputtering of particles from the surface [1–4]. Refined experimental techniques like scanning tunneling microscopy (STM), scanning force microscopy (AFM), and more extensive molecular dynamics (MD) computer simulations made it feasible to investigate also defect production at the very surface and/or in the near-surface region of ion-bombarded solids. At the surface, adatoms and vacancies may form, whereas sputtered species are emitted, typically originating from the topmost surface layer(s) [9].

The creation of adatoms on surfaces due to energetic-ion irradiation has been observed by Harrison and co-workers [15–17] in MD simulations of 5-keV Ar⁺ impact on Cu(100): a comparatively large number of atoms was relocated onto the outermost surface layer. Further observations of this phenomenon were reported in later simulations by other groups [18–20]. Snapshots from an MD simulation [21] of the evolution of a displacement cascade for 16 keV Au irradiation of Au(111) are shown in Fig. 1. The panels are cross-sections through the crystal at different times (given in the lower right) after the ion impact. The color coding indicates the atoms' kinetic energy in terms of "temperature" normalized to the melting temperature of Au ($T_m = 1338$ K). The simulations indicate that the core of the collision cascade is at temperatures above the melting point of Au for an extended time interval; this high-energy-density zone has been termed "subsurface spike" [21]. The energized material expands toward the surface, and a pronounced temporary bulge evolves. However, the material recrystallizes eventually and no crater is formed. At the end of the simulation after 20 ps (see the lowest panel in the right-hand column of Fig. 1) the atoms in the region of the cascade have almost cooled to the temperature of the surrounding atoms. However, a considerable number of adatoms are seen to remain on top of the original surface [21].

The effect of adatom formation was demonstrated experimentally using STM; several groups [22–27] have shown for a variety of materials that these and related effects of defect production are rather common phenomena under ion bombardment of surfaces. For example, the work of Michely and Comsa [28–30] illustrated by STM imaging that after 600 eV Ar⁺ bombardment of Pt(111) small monolayer-high Pt adatoms islands are formed on the original surface. The annealing of the sample at 400 K resulted in more compact adatom islands that are bounded by [110] oriented steps and have a triangular or hexagonal shape [28].

These STM experiments definitely confirmed the creation of adatoms in low-energy ion bombardments of surfaces; for low fluences, the adatom yields Y_{ad} (= number of adatoms per ion) and the sputtering yields Y_{sp} (= number of sputtered atoms per ion) have been determined [30]. A comparison with the results of associated MD simulations [19] indicates that, at low impact energies (≤ 100 eV), adatom yields are considerably higher than sputtering yields (by an order of magnitude or possibly more). At energies around 1 keV the yield ratio Y_{ad}/Y_{sp} appears to have a minimum (in the experiment) or to level off to a constant value (in the simulations).

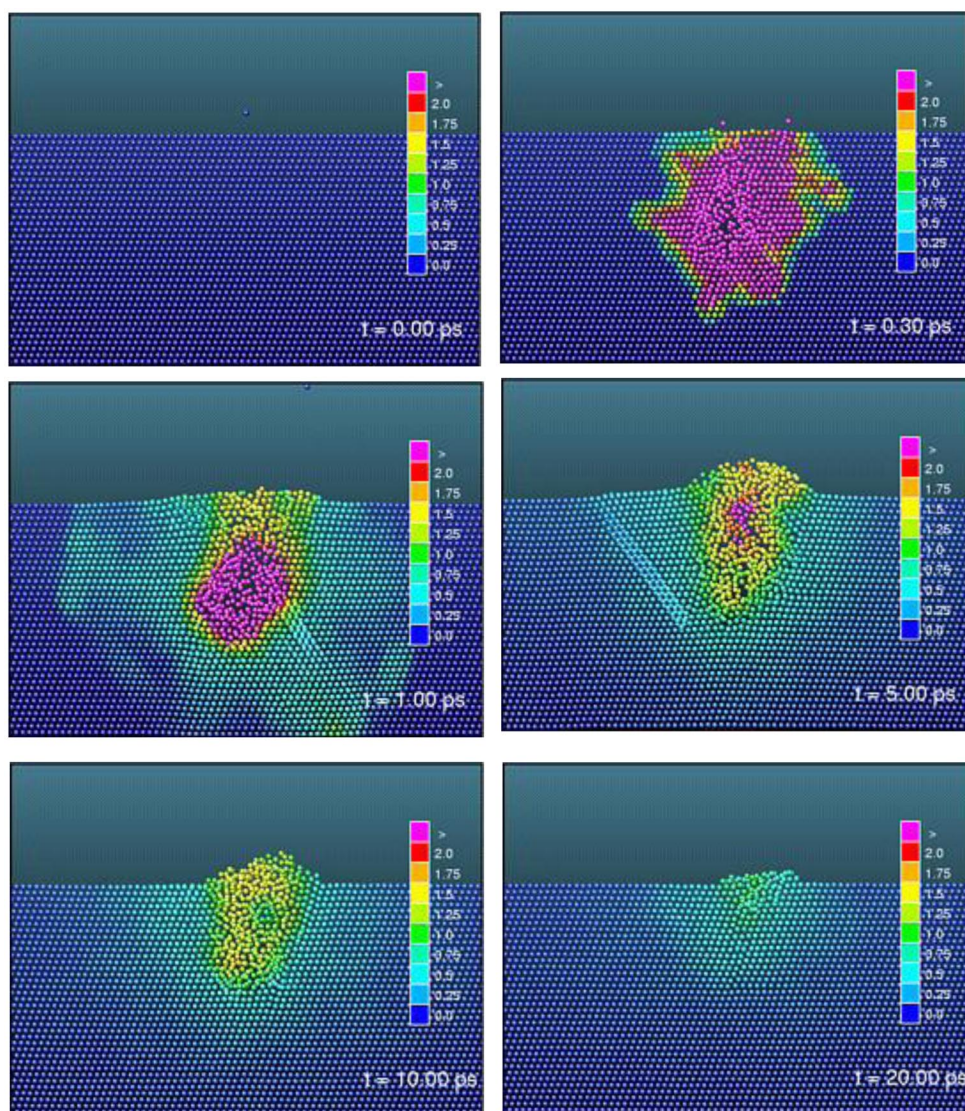


Fig. 1 Snapshots from an MD simulation of the evolution of a displacement cascade for 16 keV Au irradiation of Au(111). The panels are cross-sections through the crystal at different times (given in the lower right) after the ion impact. The color coding indicates the “temperature” normalized to the melting temperature of Au ($T_m = 1338$ K). From [21].

Using variable-temperature (20–700 K) STM, single Ne^+ , Ar^+ , Kr^+ , and Xe^+ ion impacts (at an energy of 4.5 eV) on Pt(111) were analyzed by Michely and co-workers [30,31]. The adatom yield, the number distribution of adatoms created per impact, the radial distribution of the adatoms, and the mean sizes of produced adatom and vacancy clusters were determined. Figure 2 displays the corresponding data for the adatom yields Y_{ad} and the adatom/sputtering yield ratios $Y_{\text{ad}}/Y_{\text{sp}}$ for those four ions. Ne^+ impacts (at 4.5 keV) produce only isolated adatoms with a number distribution of adatoms per impact close to a Poisson distribution. The adatom yield is compatible with a linear cascade model. At an increased energy density, corresponding to Ar^+ , Kr^+ , and Xe^+ impacts, the adatom production mechanism changes: adatom clusters with number distributions much broader than the corresponding Poisson

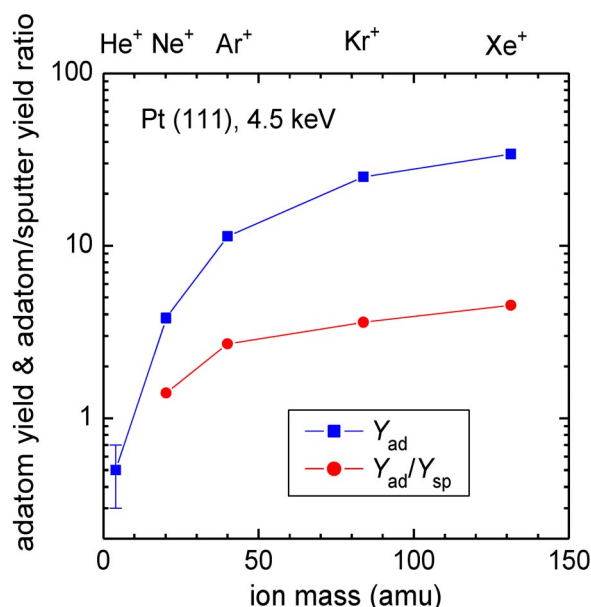


Fig. 2 Adatom yield Y_{ad} and the ratio of adatom/sputtering yield Y_{ad}/Y_{sp} as a function of ion mass for the projectiles given in the top of the figure when bombarding a Pt(111) surface. The energy was 4.5 keV, the ion fluence 5×10^{11} ions/cm². Data from [31].

distribution are created [31]. This and an increased ratio of adatom yield to sputter yield indicate that collective effects have to be taken into account to describe adatom production.

For very glancing ion-incidence angles ($\theta > 75^\circ$) on crystalline materials the ions were observed to undergo subsurface channeling, i.e., the ions may enter at a step and propagate along an open channel just beneath the surface. Using STM, damage trails were found to form by keV noble-gas ions incident onto Pt(111) [32]. Surface vacancies and adatoms aligned along the ion trajectory constitute the ion trails. MD simulations illustrate that these straight damage trails are generated by nuclear collisions with surface layer atoms during subsurface channeling of the projectiles [32]. In a small energy window (~ 5 keV), Xe⁺ ions were found to create vacancy grooves that mark the ion trajectory with atomic precision [32].

The formation of individual surface defects under ion irradiation has also been studied extensively for semiconductors [33–38]. For example, low-fluence experiments on the reconstructed Si(111)-(7 × 7) and Si(100)-(2 × 1) surfaces of silicon were performed by Zandvliet et al. [33,34], monitoring the surfaces by means of STM. For 3 keV Ar⁺ bombardment and fluences of $\leq 6 \times 10^{12}$ ions/cm², defects created by ion impact are mainly in the form of missing atoms. These vacancies tend to congregate to give the appearance of craters. In the vicinity of these craters, some bright features were found. Most probably these are adatoms (or adclusters) which originate from the emission process.

Surface defects created on Ge(100) by exposure to very low energy ($20 \leq E \leq 240$ eV) Xe⁺ ions were examined by Cahill and co-workers [36,37] employing STM imaging. These experiments were carried out at a sample temperature of 440 K, since Ge remains crystalline under ion bombardment at those low energies. Ion impacts generate defects (vacancies and adatoms), which nucleate and form vacancy and adatom islands. Generally, for a fixed total number of created vacancies, the vacancy island number density increases with increasing ion energy, whereas the vacancy island size decreases. From the STM micrographs, the authors determined the yield of vacancies and adatoms as a function of ion energy [37]. These data are shown in Fig. 3. For an ion energy from 40 to 240 eV, the ratio of adatoms-to-vacancies is roughly constant, $\sim 0.14 \pm 0.03$, but increases to 0.85 ± 0.17 at 20 eV ion impact. This

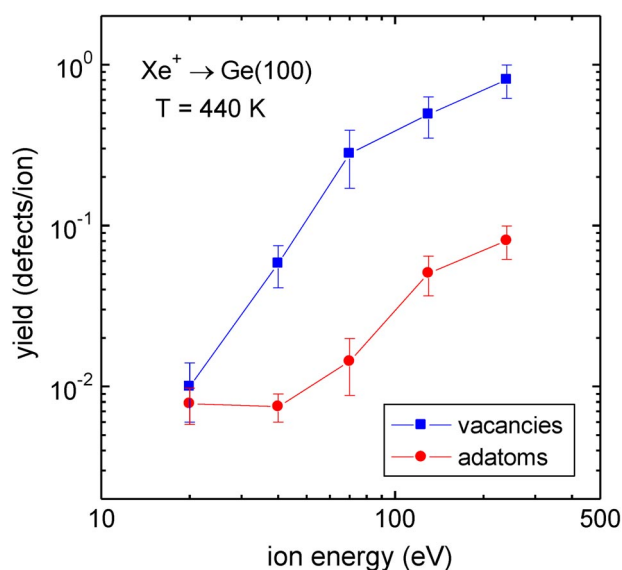


Fig. 3 The yield of adatom and vacancy creation per incident ion as a function of ion energy for Xe^+ ion bombardment of Ge(100) at a specimen temperature of 440 K. The yields were derived from STM images. Data from [37].

defect production includes the annihilation of adatom-vacancy pairs due to the finite defect mobility at 440 K. Similarly, they derived the total sputtering yield in the investigated Xe^+ ion energy range: Y_{sp} increases from $\sim 10^{-3}$ Ge-atoms/ Xe^+ at 20 eV to about 0.7 at 240 eV.

The temperature dependence of the defect yield on Ge(001) surfaces was measured using in situ reflection high-energy electron diffraction [39] and demonstrated the presence of defect recombination. At low temperatures (< 270 K), mobile bulk defects diffuse to the surface, where they become immobile; the measured surface defect yield is comparable to the total number of ion-induced defects produced. Above 300 K, surface recombination processes become more active, and the total number of surface defects drops rapidly (by a factor of ~ 10) to a constant value at temperatures > 370 K [39].

STM investigations of ion-bombarded GaAs(110) surfaces were carried out by Weaver and co-workers [40–42], using Ar^+ and Xe^+ ions with energies from 300 eV to 5 keV. Figure 4a shows an STM image from that work taken after bombarding the surface at 300 K with 3 keV Ar^+ at normal incidence with a fluence of 5.4×10^{12} ions/ cm^2 [40]. Pits (craters) of one or a few missing atoms, adatoms ejected on the surface, and disordered regions are produced by ion irradiation. Most of the observed surface layer defects span 1–5 unit cells (the unit cell has a size of 0.4×0.56 nm 2) at low fluences (10^{12} – 10^{13} ions/ cm^2) and room-temperature bombardment. Ion irradiation of GaAs at elevated temperatures (625–775 K) shows [40,41] that adatom diffusion and adatom-vacancy annihilation processes occur, and vacancy migration and coalescence become apparent. Figure 4b shows an STM image of a GaAs(110) surface bombarded at 625 K by 300 eV Ar^+ ions [41]; the ion flux amounted to 3×10^{11} cm $^{-2}$ s $^{-1}$ which corresponded to the removal of ~ 0.05 ML. The images reveal that monolayer-deep vacancy islands are the dominant structures, but with very few adatoms ejected onto the surface (the bright features in Fig. 4b). The lateral dimension of these islands increased with temperature, and their density decreased.

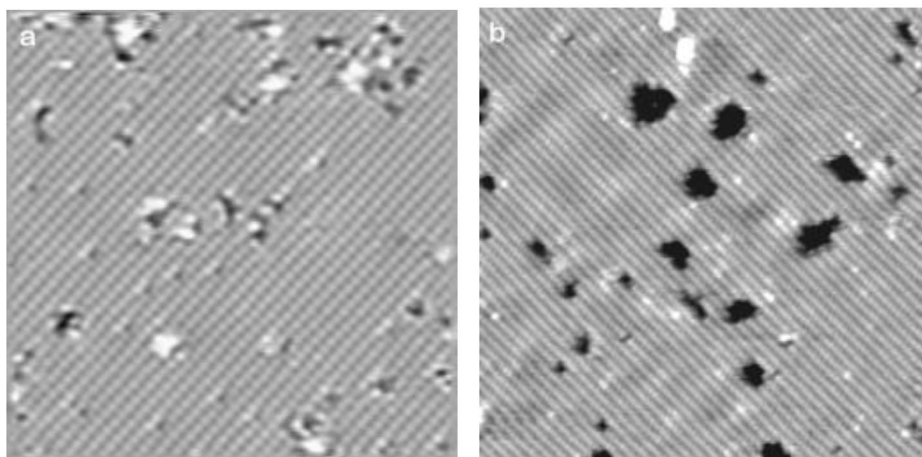


Fig. 4 STM images of GaAs(110) after ion bombardment with (a) 3-keV Ar^+ ions at a sample temperature of 300 K (ion fluence 5.4×10^{12} ions/cm², scan area 20×20 nm²) and (b) 300-eV Ar^+ at a sample temperature of 625 K (ion flux 3×10^{11} ions/cm² s⁻¹, ~ 0.05 ML removed, scan area 25×25 nm²). In the upper right of (a) defects extending over up to 20 unit cells are seen, whereas in (b) single-layer-deep vacancy and adatom islands (black and white regions, respectively) are visible. Adapted from [40,41].

TRANSITION TO EXTENDED SURFACE DAMAGE AND MULTILAYER REMOVAL

The low-fluence ion bombardment regime discussed in the previous section produces isolated surface defects (vacancies, adatoms) which, at room temperature, are frozen out and do not interact. At elevated temperatures, however, these defects tend to form adatom and vacancy islands. The surface morphology that develops during ion bombardment at fluences beyond those single-ion impacts might depend in a complex way on irradiation- and specimen-related parameters. Eventually, pronounced topographic features may evolve at ion-bombarded surfaces for (very) high fluence. This section will illustrate the transition from the generation of isolated surface defects (adatoms and vacancies) and small defect clusters to the initial stages of the formation of gross surface defect structures, whereas the fourth section will describe the latter features.

The evolution of surface morphology can be characterized by the interface (surface) width w , which is given by [12,43]

$$w(L,t) \equiv \frac{1}{L} \sqrt{\sum_{x,y=1}^L [h(x,y,t) - \bar{h}(t)]^2} \quad (1)$$

where $h(x,y,t)$ is the height at position (x,y) , \bar{h} denotes the mean surface height over the linear system size L , and t is the duration of sputtering (i.e., a measure of the ion fluence and, hence, of the material removed). The interface width may exhibit a general scaling behavior [44,45]

$$w(L,t) \propto t^\beta \quad (2)$$

for $t < t_c$ with the growth exponent β , and

$$w_{\text{sat}}(L,t) \propto L^\alpha \quad (3)$$

for $t > t_c$ with the roughness exponent α . α and β are correlated with the “crossover time” t_c via the dynamic exponent z

$$t_c \propto L^z \quad (4)$$

with $z = \alpha/\beta$. Generally, this may result in a scaling relation for the interface width $w(L,t)$

$$w(L,t) \propto L^\alpha f\left(\frac{t}{L^z}\right) \quad (5)$$

with the scaling function

$$\begin{array}{ll} f(u) \propto u^\beta & \text{for } u \ll 1 \\ f(u) \propto \text{const} & \text{for } u \gg 1 \end{array}$$

The exponents α, β define a universality class and are related to the surface transport mechanisms. (For a general discussion see, e.g., [43,46,47]). Figure 5 illustrates these correlations in general terms. They might be applied to the evaluation of experimental data as will be shown in the following.

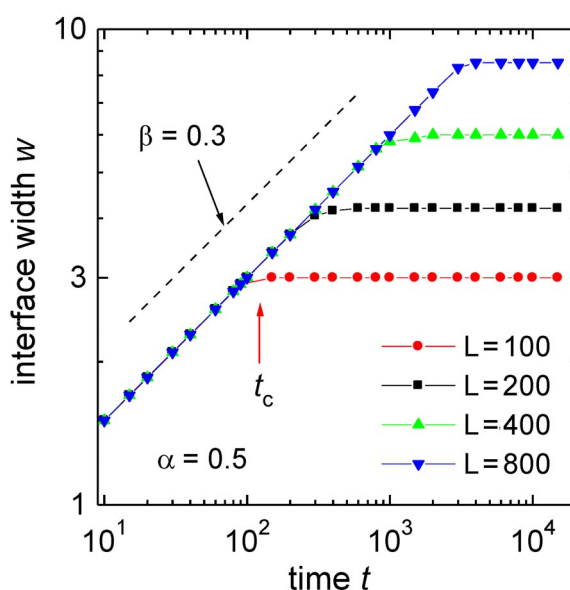


Fig. 5 The interface width w as a function of irradiation time t , computed according to eqs. 1–4 with $\alpha = 0.5$ and $\beta = 0.3$. The parameter is the system size L . The crossover time t_c is seen to depend on L .

Multilayer erosion of a GaAs(110) surface by 0.3–3 keV Ar^+ and Xe^+ ions at temperatures between 625 and 775 K was investigated by Weaver and co-workers [40–42] employing STM imaging. Figure 6 shows STM images [42] from a GaAs(110) surface irradiated by 2 keV Xe^+ ions at 725 K (images a and b) and at 625 K (c and d). The amount of material removed corresponds to 1.4 ML in Fig. 6a, with about 3 % of the original top layer remaining as isolated monolayer islands. Vacancy islands as large as 30 nm appear in the second layer. The interface width w is 0.6 ML. Removing 10 ML at 725 K, Fig. 6b, results in $w = 1.8$ ML, with up to 10 layers exposed. At 625 K, the surface roughness evolves in a different way. The surface width w grows rapidly, and the step density increases quickly by the formation of many small-sized and rough-edged vacancy islands, cf. Figs. 6c,d. Values of w are 0.9 and 1.8 ML at, respectively, 1.8 and 10 ML removed [42].

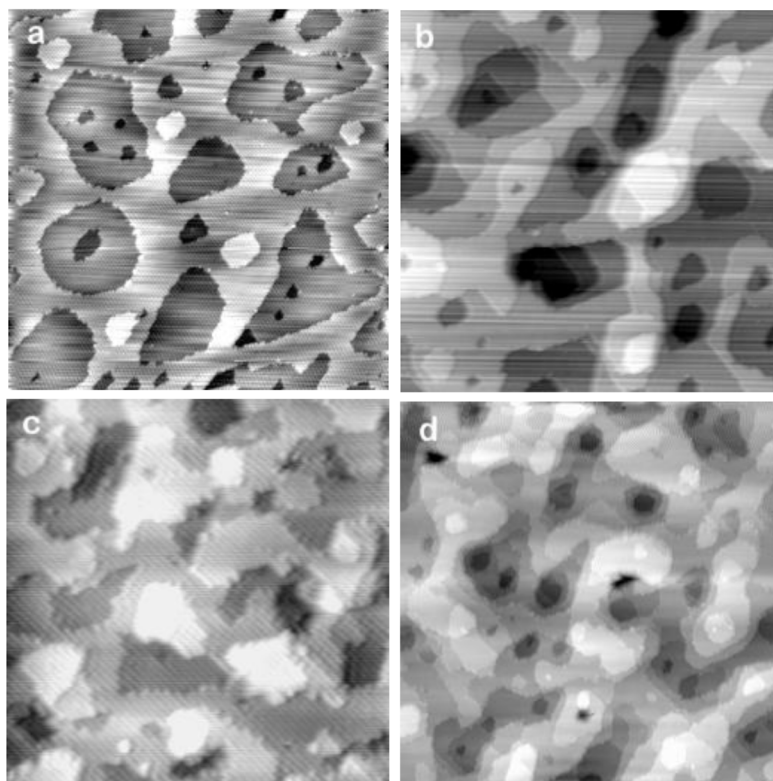


Fig. 6 STM images of GaAs(110) after 2 keV Xe⁺ ion irradiation at 725 K (a,b), and 625 K (c,d). Image sizes are 90 × 90 nm² (a), 45 × 45 nm² (c), and 108 × 108 nm² (b,d). The material removed is 1.4 ML (a), 1.8 ML (c), and 10 ML (b,d). Adapted from [42].

This group [42] determined for each temperature and t the values of w as a function of sampling size L . These data are shown in Fig. 7. Generally, w increases initially with L and reaches saturation at L_c . For $L < L_c$ the data can be fitted with L^α , where $\alpha = 0.38$. The values of L_c increase linearly with increasing t in the range studied in the experiment (1–10 ML); the increase is faster at the higher temperature. The authors [42] summarize their findings by noting that after removal of 10 monolayers at 625 K the surfaces are rougher on a small scale than those at 725 K, but they are smoother on a large scale. The increased large-scale roughness at high T was ascribed to increased diffusion on terraces and along step edges, but insufficient cross-step transport. Generally, the short-range surface width is related to step density, which is determined by *intralayer* diffusion, whereas the long-range width depends on *interlayer* mass transport [42]. The high step density created at low T *enhanced* cross-step transport, thereby *reducing* large-scale roughness. The surface width at 725 K increases as $w \propto t^\beta$ with $\beta = 0.3$. Such a dependence is consistent with a “growth” law [47], whereby the interface width increases with deposition time during deposition at a constant flux, the growth exponent β depending on temperature. In multilayer erosion, β is a measure of the effectiveness of interlayer transport. (If there is no such transport, then $\beta = 0.5$. For layer-by-layer sputtering, $\beta = 0$.) Conversely, at 625 K no such simple relationship was valid and $\beta > 0.3$ for $t < 1$ ML and $\beta < 0.3$ for $t > 1$ ML was observed [42].

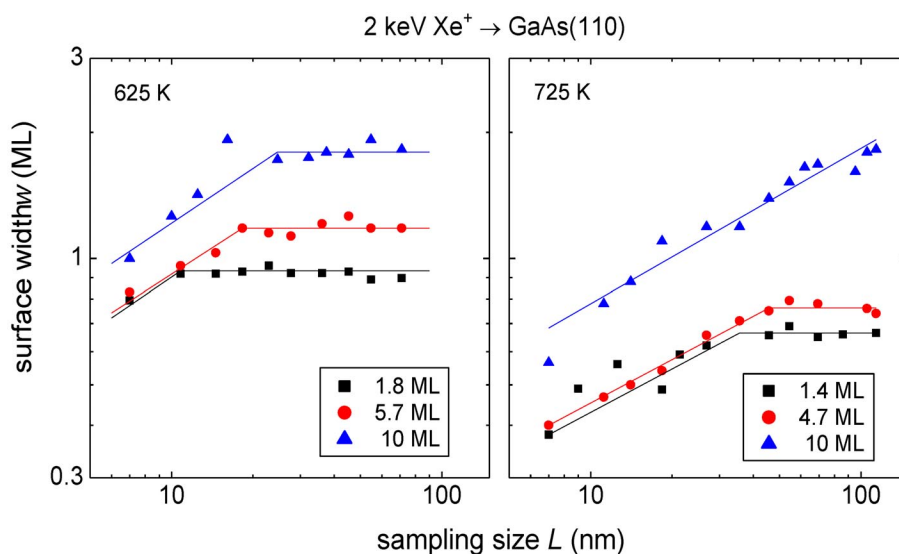


Fig. 7 Surface width as a function of sampling size for different amounts of material removal at 625 and 725 K. Above L_c the surface width saturates at the large-scale value. Data from [42].

The temperature-dependent morphological evolution of Pt(111) under 1 keV Xe^+ normal-incidence ion bombardment has been investigated up to the removal of 600 monolayers [29,48–50]. Figures 8a–d display STM topographs upon the removal of an increasing number of surface layers at a temperature of 600 K [49]. The morphology develops from monolayer deep compact vacancy islands to regular hexagonal pits consisting of stacked vacancy islands and remaining pyramids and ridges in between. This evolution is driven by preferential nucleation of new vacancy islands at the bottom of existing ones. Figures 8e–h exhibit STM topographs (note the different scale) after removal of similar amounts of material, but at 750 K. In contrast to the erosion at 600 K, at 750 K vacancy islands initially coalesce

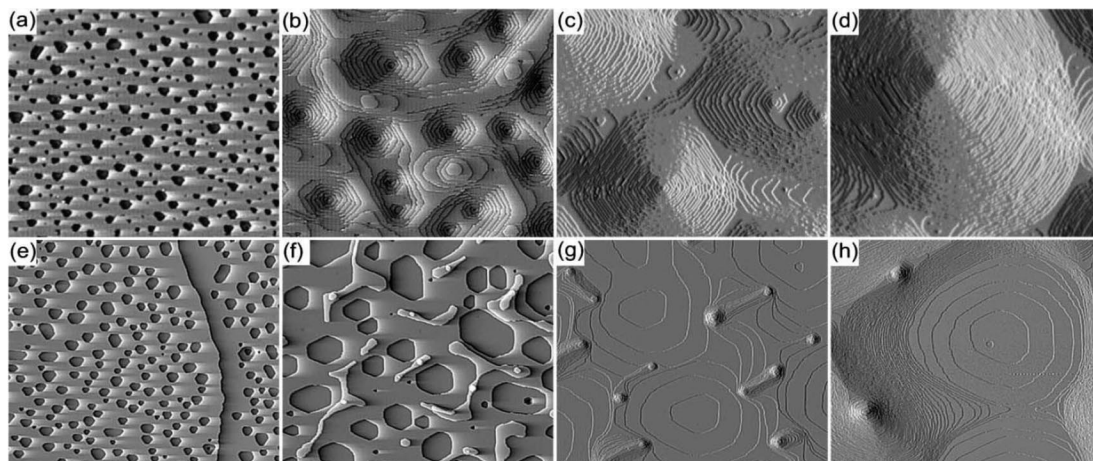


Fig. 8 STM topography images of a Pt(111) surface after erosion, by 1 keV Xe^+ ions of (a) 0.26 ML, (b) 6.2 ML, (c) 66 ML, and (d) 333 ML at 600 K, and of (e) 0.24 ML, (f) 6.3 ML, (g) 65 ML, and (h) 601 ML at 750 K. Image width 81 nm for (a–d) and 346 nm for (e–h). From [49].

prior to nucleation of new vacancy islands on the bottom terraces. The experiments demonstrate that there is a large difference in roughness evolution at the two temperatures: At 600 K roughness increases rapidly with the amount removed θ and for $\theta > 10$ ML a scaling exponent $\beta = 0.34$ (roughness $\sigma \propto \theta^\beta$) is obtained. Although at 750 K and for $\theta > 10$ ML roughness increases faster than at 600 K (signified by $\beta = 0.57$), due to the delay in roughness build-up the absolute values of roughness remain lower. The authors [49,50] argue that the coarsening of the surface structures during erosion and the qualitative change in roughness evolution between 650 and 700 K are caused by different atomic processes: the former by diffusion of atoms along steps, the latter by the onset of step atom detachment.

The onset of pattern formation at grazing incidence was investigated by STM for Pt(111) surfaces under 5 keV Ar⁺ ion bombardment for a broad temperature range (100–720 K) and supplemented by MD simulations of single-ion impacts [51–53]. The experiments indicate that pattern formation depends crucially on the angle of incidence of the ions. At very glancing incidence (θ greater than $\sim 80^\circ$), planar subsurface channeling of the ions may occur [32]. In the absence of subsurface channeling, pattern alignment is due to the preferential removal of step edges illuminated by the ion beam. However, if the angle of ion incidence allows subsurface channeling with significant probability, pattern alignment and regularity were found to greatly improve due to the aligned formation and coalescence of vacancy islands as a consequence of the dechanneling damage of single ions [53]. In terms of temperature dependence, the experiments show a distinction between an athermal (200–500 K) and a thermal (500–700 K) pattern formation regime. Below 200 K and above 700 K, pattern formation ceases due to the dominance of noise and due to adatom lattice gas formation, respectively [52].

ORDERED NANOPATTERNS ON SURFACES BY ION BOMBARDMENT

Upon prolonged ion irradiation, a stationary morphology of the surface may evolve. Very often, the development of highly periodic structures with nanoscale dimensions (such as “nanodots” and “ripple”-like morphologies) has been observed. Different types of patterns were observed to develop under different conditions, with characteristic features that depend on the substrate material, the ion-beam parameters, and the processing conditions. This wide variety of surface morphologies has been the subject of extensive theoretical and experimental studies over the past decade (see [11–14] for recent reviews). Generally, these phenomena are believed to be related to (and caused by) the interplay between ion erosion (which roughens the surface) and transport processes (diffusion) which induce a smoothing. In the following, some examples for such features will be presented and the pertinent theoretical concepts will be outlined.

The first observations of the formation fairly regular ripple patterns on surfaces under ion irradiation date back to the early 1960s [54,55]. Bombarding a glass surface with a keV ion beam of air, wavelike structures were observed with wavelengths between 30 and 120 nm [55]; their orientation was found to depend on the incidence angle of the ions with respect to the surface normal, θ : the ripples align perpendicularly to the beam for $\theta = 30^\circ$, whereas they align along the beam at $\theta = 80^\circ$. In fact, this change in orientation has been observed in many later experiments. For example, the topography of (0001)-graphite (highly oriented pyrolytic graphite, HOPG) surfaces eroded by a 5 keV Xe⁺ ion beam has been investigated using STM [56,57]. For tilted incidence of the ion beam and ion fluences of about 10^{17} cm⁻², a quasi-periodic ripple topography with characteristic wavelengths between 40 and 70 nm has been found. Below a critical incidence angle θ_c the ripples are oriented perpendicular to the ion-beam projection onto the surface, while for angles above θ_c the ripple orientation is parallel to the ion-beam projection. The critical angle θ_c lies between 60° and 70° [56]. Figure 9 illustrates this finding for 5 keV Xe⁺ bombardment at $\theta = 30^\circ$, 60° , and 70° . The authors show [56] that these results are in agreement with the predictions of a continuum theory and that for increasing ion fluences, large-scale perturbations of the surface topography occur, indicating a nonlinear behavior. These theoretical concepts will be discussed below.

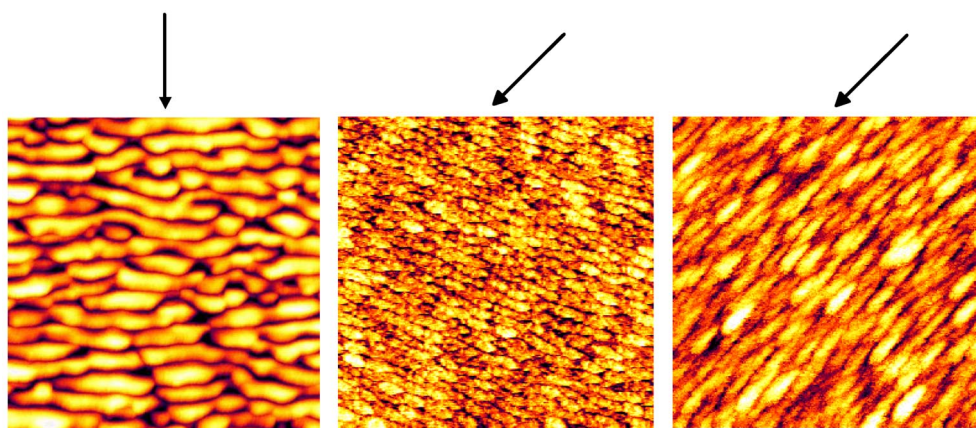


Fig. 9 STM topography images ($1\ \mu\text{m} \times 1\ \mu\text{m}$) of a HOPG surfaces eroded by 5 keV Xe^+ ions with at a fluence $3 \times 10^{17}\ \text{ions/cm}^2$; the incident angles were $\theta = 30^\circ$ (left), $\theta = 60^\circ$ (center), and $\theta = 70^\circ$ (right). The arrows indicate the direction of the ion beam. Adapted from [56].

The occurrence of regular ripple pattern has been studied extensively for various metal surfaces [58–68]. For example, the evolution of the Cu(110) surface morphology during low-temperature (180 K) ion sputtering was studied as a function of the incident ion-beam angle θ by means of STM [60]. The morphology was dominated by a ripple structure with the wave vector parallel or perpendicular to the direction of the incident beam. STM images of the Cu(110) surface taken at different bombarding fluences showed that the ripple wavelength is increasing with fluence. Figure 10 displays this dependence. The time evolution of the interface shows that the ripple wavelength increases with time

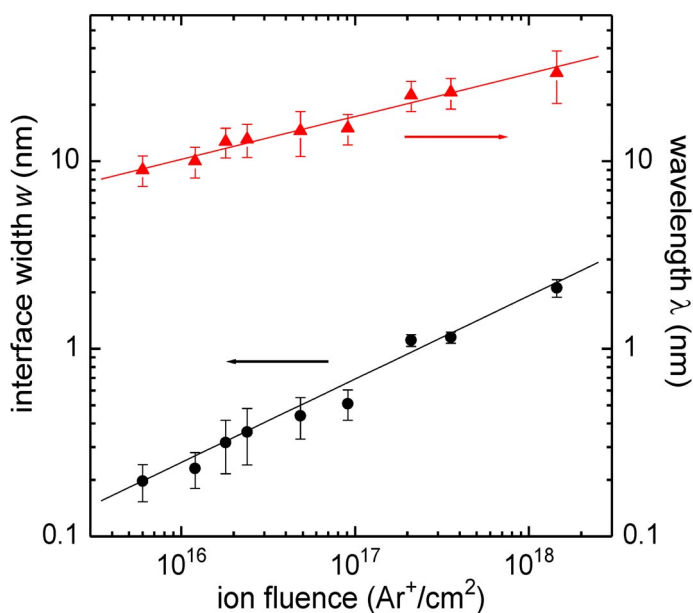


Fig. 10 The ripple wavelength λ and the interface width w as a function of the ion fluence for a Cu(110) surface under 1 keV Ar^+ ion bombardment. Sample temperature $T = 180\ \text{K}$, ion incidence $\theta = 45^\circ$, and the current density is $16\ \mu\text{A/cm}^2$. Data from [60].

following a scaling law $\lambda \sim t^z$, with $z = 0.26 \pm 0.02$. The interface width w was found to scale as $w \sim t^\beta$, with $\beta = 0.43 \pm 0.08$ [60]. These authors conclude from their results [60] that for a full description of the erosion process on single crystal metals it is necessary to introduce in the theoretical models a realistic diffusion term, taking into account the presence of a Schwoebel barrier as it is familiar in film growth.

Very well ordered nanostructures have been observed on semiconductor surfaces and the evolution of these features and their dependence on various ion-beam parameters has been studied in considerable detail [69–85]. For a given material, the type of pattern that is created may depend pronouncedly on the ion's energy and incidence angle. This finding is very clearly illustrated in Fig. 11, which displays AFM images of a Ge surface bombardment by 2 keV Xe^+ ions at incidence angles θ of 0° , 5° , 10° , and 20° [82]. There is first a transition from dots to ripples and then back from ripples to dots with increasing ion incidence angle. The AFM image for normal incidence in Fig. 11 shows dot structures, whereas at $\theta = 5^\circ$ the dot nanostructures disappear and well-ordered parallel mode ripples evolve on the surface. By increasing the ion incidence angle to 10° ripples, having a curved form, are still dominating the surface, but they start to transform into dots. Further increase of θ toward 20° results in a complete transition from ripple to dot pattern and the dots have a hexagonal ordering within the whole image area. The corresponding fast Fourier transform (FFT) image shows six equidistant peaks [82].

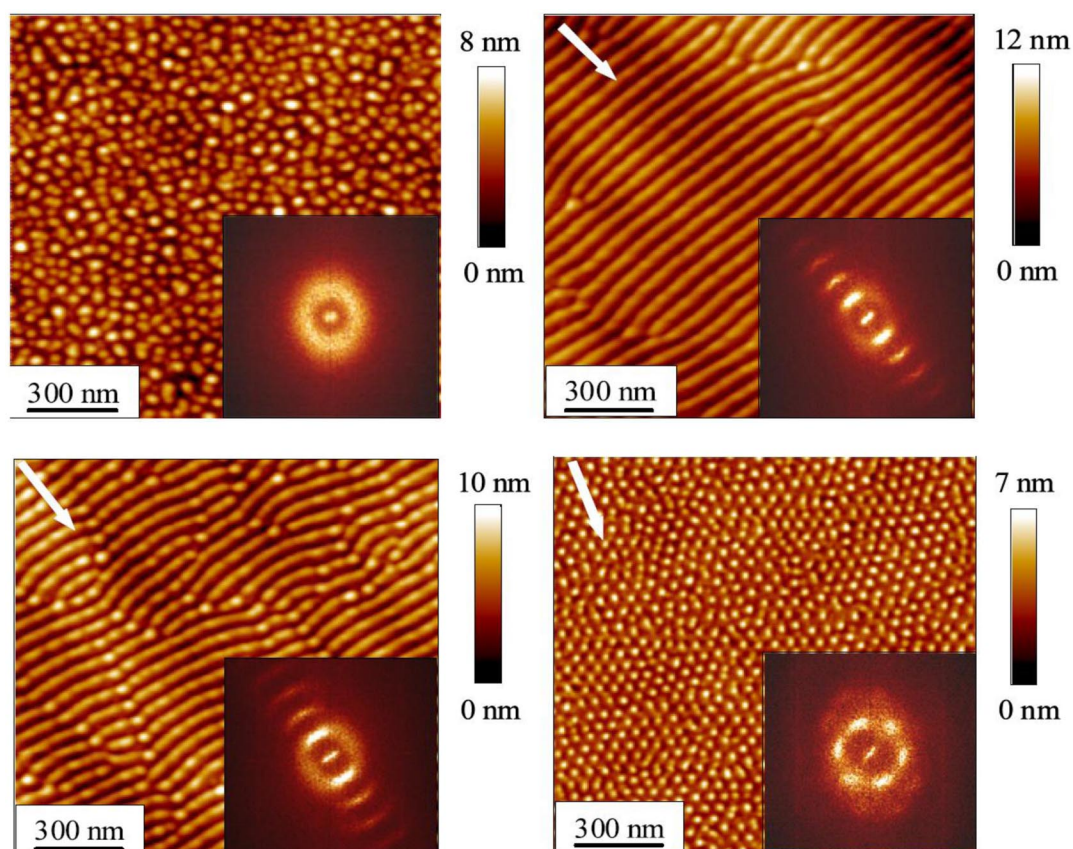


Fig. 11 Surface topography (AFM images) on Ge after 2 keV Xe^+ ion-beam erosion for different ion incidence angles ($\theta = 0^\circ$, 5° , 10° , and 20° , clockwise from top left). The arrows give the ion-beam direction. Inset: corresponding FFT images calculated from the AFM images having $4 \mu\text{m} \times 4 \mu\text{m}$ size. From [82].

The transition from ripples to dots and vice versa is also found for Si surfaces at specific incidence angles. For certain values of θ , dots show an almost perfect lateral ordering, with only a few defects, see Fig. 12 [82]. The corresponding FFT image confirms the square ordering of dots (the white arrows in Fig. 12 point out the two distinct wave vectors).

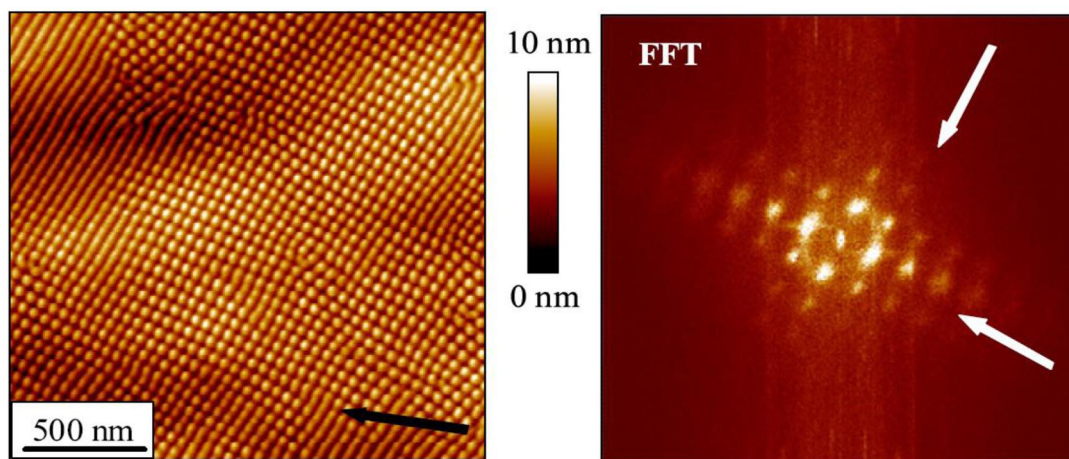


Fig. 12 An almost perfect square array of dots on an Si surface (2 keV Xe⁺, $\theta = 26^\circ$), where the black arrow in the AFM image (left panel) indicates the ion-beam direction. The corresponding FFT image (right panel) confirms the square ordering of dots (the white arrows point out the two distinct wave vectors). From [82].

As an adequate representation, the evolution of the surface topography with different ion energy E_{ion} and incidence angle α_{ion} are plotted in a *topography diagram* (TD). Such a TD is presented for Si and Ge in Fig. 13 [82]. Each symbol represents a typical topography. It reveals the different evolving topographies that depend on E_{ion} and α_{ion} . The boundaries (solid and dotted lines) on the TD distinguish between different topography regions. These results for Si and Ge show that the ion energy is a key parameter for pattern formation and for establishing the periodicity. Generally, the results show an increase of the wavelength of nanostructures and their amplitude with ion energy [82].

While the development of such nanostructures on surfaces exposed to ion irradiation appears to be a rather ubiquitous phenomenon, it was noted recently that impurities may influence pattern formation [86–95]. For example, Mo atoms co-sputtered from sample clips during ion irradiation were found to foster dot formation on Si under normal incidence bombardment [86,88,91]. Recent systematic studies [93–95] examined pattern formation while varying the concentration of Fe atoms on Si surfaces. For clean surfaces, no ion-beam patterns were found to form for incidence angles $\theta \leq 45^\circ$; rather, the ion beam induces a smoothing of preformed patterns [93]. On the other hand, the presence of Fe atoms results, in that angular range, in the formation of a variety of patterns; their specific features were observed to depend on the amount of Fe on the surface. This surfactant-driven self-organization may constitute a versatile approach for creating novel nanopatterns on surfaces [94].

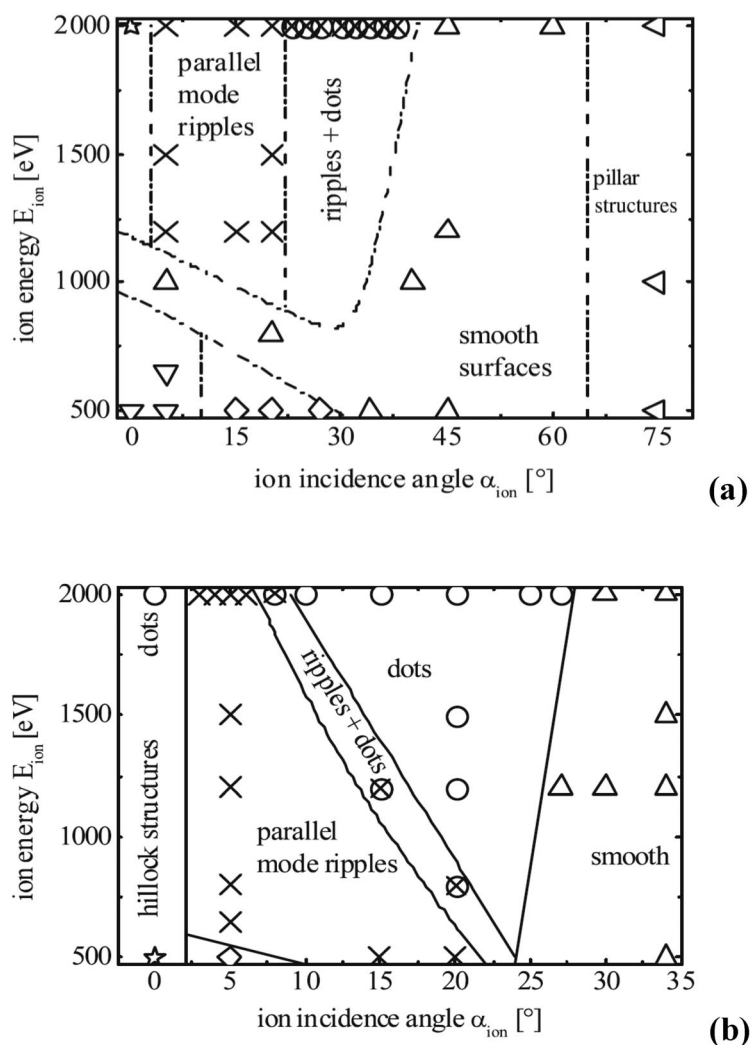


Fig. 13 Topography diagrams showing the surface topography on (a) Si and (b) Ge due to Xe^+ ion-beam erosion for different ion energies and ion incidence angles. The symbols indicate the different structures observed: smooth surfaces, hillock structures, perpendicular-mode ripples, parallel-mode ripples, parallel-mode ripples + dots, columnar structures, and dots. From [82].

Nanostructures on surfaces have commonly been investigated ex situ, using STM, AFM, scanning electron microscopy (SEM), or other techniques [96–106]. Any possible (lateral) movement with increasing ion fluence cannot easily be detected in such a way. Only a few experiments [107–110] have been carried out in situ, that is, by monitoring the irradiated area without removing the specimen from the ion-bombardment system. A focused ion beam (FIB) system was recently employed [110] to investigate such a ripple movement: this dual-beam instrument features a finely focused Ga^+ ion beam and an electron beam. A glass surface was irradiated by 30 keV Ga^+ ions (incidence angle $\theta = 52^\circ$) and, without sample movement, the area hit by the ions could be monitored by SEM (incidence angle of the electron beam is 0°). Taking SEM images at different ion fluences, the movement of the ripples could be determined. Figure 14 shows some of these images [110]. With increasing ion fluence, the ripples

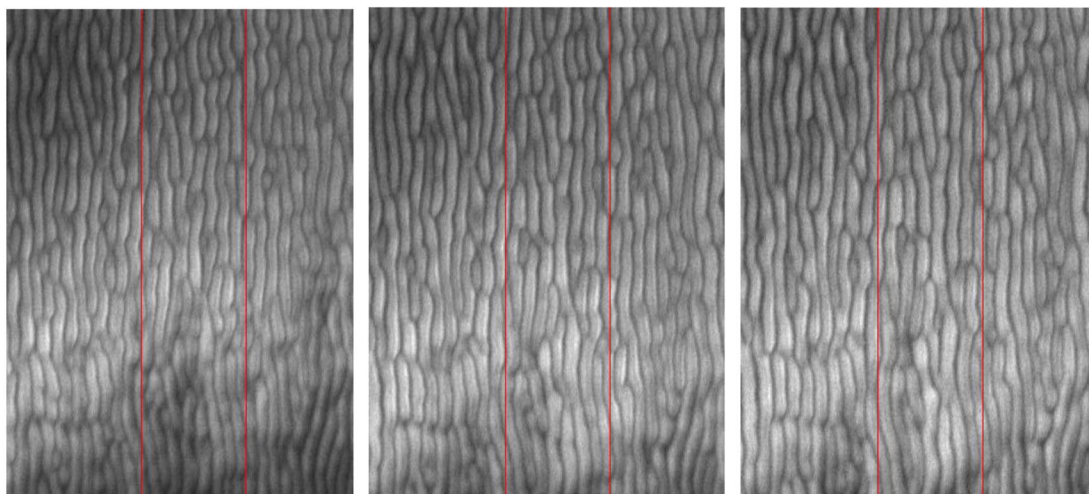


Fig. 14 AFM images of the ripple structure on a glass surface bombarded by 30 keV Ga^+ ions in an FIB. The ions' incidence angle was 52° and the incidence direction was from the left. The fluences amounted to $3 \times 10^{17} \text{ cm}^{-2}$ (left-hand image), $4 \times 10^{17} \text{ cm}^{-2}$ (center image) and $5 \times 10^{17} \text{ cm}^{-2}$ (right-hand image). The images were taken with the SEM directly in the instrument. The vertical lines in each image refer to marker outside of the irradiated area; they have a distance of $2.04 \mu\text{m}$. With increasing fluence, the images show a propagation of the ripples to the right. From [110].

were found to move in the direction of the incident ion beam (to the right in Fig. 14) and the propagation velocity was found to be $\sim 60 \text{ nm}/10^{17} \text{ Ga}^+ \text{ ions cm}^{-2}$. The wavelength of the ripples is $\sim 270 \text{ nm}$.

THEORETICAL MODELS OF SURFACE NANOPATTERNING

The examples in the previous section demonstrate that when beams of low-energy ions are used to bombard materials, the surface often develops a periodic pattern or “ripple” structure. It was seen that different types of patterns are observed to develop under different conditions, with characteristic features that depend on the substrate material, the ion-beam parameters, and the processing conditions. Because the patterns develop spontaneously, without applying any external mask or template, their formation is the expression of a dynamic balance among fundamental surface kinetic processes, e.g., erosion of material from the surface, ion-induced defect creation, and defect-mediated evolution of the surface morphology [14]. Initial theoretical modeling showed that the description of the surface morphology may then be done via continuum equations that take into account the above-mentioned effects contributing to an equilibrium state [111]. Several extensions and modifications of this Bradley–Harper model were later proposed [112–115]. A possible ansatz is the anisotropic noisy Kuramoto–Sivashinsky (KS) equation [116–120]

$$\begin{aligned}
 \frac{\partial h}{\partial t} = & \underbrace{-v_0 + \gamma \frac{\partial h}{\partial x}}_A + \underbrace{v_x \frac{\partial^2 h}{\partial x^2} + v_y \frac{\partial^2 h}{\partial y^2}}_B + \underbrace{\frac{\lambda_x}{2} \left(\frac{\partial h}{\partial x} \right)^2 + \frac{\lambda_y}{2} \left(\frac{\partial h}{\partial y} \right)^2}_C - \\
 & \underbrace{D_x \frac{\partial^4 h}{\partial x^4} - D_y \frac{\partial^4 h}{\partial y^4}}_D + \underbrace{\eta(\vec{r}, t)}_E
 \end{aligned} \tag{6}$$

Here, v_0 is the overall erosion rate, the second term in A accounts for the motion of surface features along the x direction in the presence of a local curvature with γ being the derivative of the erosion rate with respect to the ions' incidence angle [121], v_x and v_y (in B) represent ion-induced surface tension terms, λ_x and λ_y (in C) characterize the slope dependence of the erosion rate, while D_x and D_y are the general diffusion coefficients. Term E is a noise term that takes into account the stochastic arrival of ions.

At a given temperature, the total diffusion constant is given by contributions due to thermal diffusion and ion-induced diffusion, $D = D_I + D_T$. As the sample temperature T decreases, there is critical temperature T_c at which $D_I = D_T$, so that for $T < T_c$ the diffusion is dominated by its ion-induced component, which is independent of temperature.

The origin of the ripple formation during ion sputtering is an ion-induced instability [122,123]: valleys are eroded faster than crests, expressed by negative v_x and v_y coefficients in eq. 6 [111]. At short wavelength this instability is balanced by surface diffusion; hence, a competition between roughening (curvature-dependent erosion) and smoothing exists. A linear stability analysis predicts that the observable ripple wavelength is

$$\Lambda = 2\pi\sqrt{D/|v|} \quad (7)$$

where v is the largest in absolute value of the negative surface tension coefficients. Accordingly, the wave vector of the ripples is parallel to the x axis for small θ and perpendicular to it for large θ [111].

If values of the various parameters entering eq. 6 are known or can be estimated, a morphological phase diagram can be constructed which would indicate the kind of surface morphology that may develop. Figure 15 exemplifies such a diagram [119]. The pronounced dependence on ion-beam parameters and diffusion coefficients is obvious.

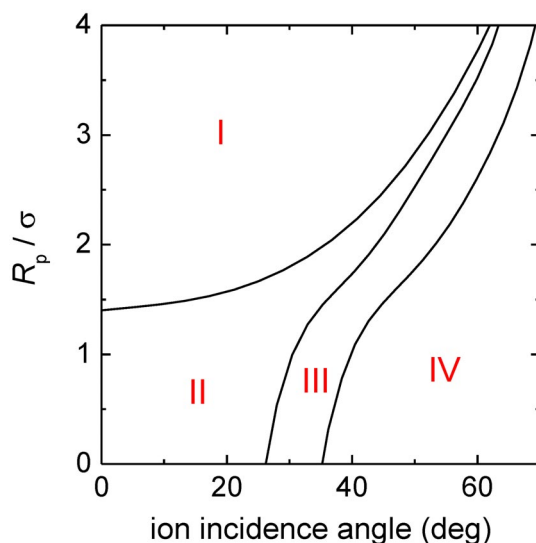


Fig. 15 Computed-phase diagram depicting the surface morphology that may develop for specific parameters in eq. 6. R_p is the projected range of the ions, and σ is the straggling of the range. Region I: $v_x, v_y < 0$ and $D_x, D_y > 0$, superimposed ripples in x - and y -directions, but $\Lambda_x > \Lambda_y$, therefore, the y -direction may dominate. Region II: $v_x, v_y < 0$ and $D_x, D_y > 0$, $\Lambda_x < \Lambda_y$, and ripple wave vector along x -direction. Region III: $v_x, v_y < 0$, $D_x < 0$, $D_y > 0$, system unstable at large length scales. Region IV: $v_x > 0$, $v_y < 0$, $D_x < 0$, $D_y > 0$, ripple wave vector along y -direction. Data from [119].

Whereas the damped or undamped KS equations often show a good qualitative agreement with many experimental findings, they still fail to predict several other important observations [14,124]. Different other concepts have therefore been proposed [125–128]. For example, some improvement has been achieved by including the mass rearrangement on the surface induced by the ion impact [129,130]. Other models go beyond the KS equations and introduce coupled fields for the mobile species [131–133] or the concentrations of the elements in compound materials [134].

OTHER NANOSTRUCTURES CREATED BY ION IRRADIATION

FIB systems [135,136] have developed now into indispensable tools for many processes of great technological importance [137,138]. Typically, FIBs are based on liquid-metal ion sources (LMIS) forming Ga^+ ion beams; because of the very high brightness ($>10^6 \text{ A/cm}^2 \text{ sr}$) and small virtual source size ($<100 \text{ nm}$) [139,140] of LIMS, very small spot sizes ($\sim 10 \text{ nm}$) and extremely high current densities ($>1 \text{ A/cm}^2$) can be achieved using suitable electrostatic focusing columns. These irradiation conditions may lead to the formation of quite specific surface structures [137,141–147].

For example, it was observed that nanodroplets can form on a GaAs surface under off-normal bombardment by 5 keV Ga^+ ions [148]. These droplets have sizes from 70 to 25 nm in diameter and can self-assemble into highly ordered hexagonal pattern instead of Ostwald ripening or coalescence. The mechanism proposed [148] for the evolution of these structures relies on a balance between an anisotropic loss of atoms on the surface of droplets due to sputtering and an anisotropic supply of atoms (mass transport) due to the oblique ion incidence. The periodic patterning was envisaged to proceed in a way similar to the formation of highly ordered colloidal particles, with the radius of the droplets reaching eventually a stationary state. In a subsequent investigation [149] the formation and coarsening of Ga droplets on GaAs surfaces irradiated by 10–30 keV Ga^+ ions from an FIB was examined and the droplet growth rate and size distribution was determined as a function of ion energy. The data suggest a droplet formation mechanism that involves Ga precipitation from an ion-induced Ga-rich surface layer [149]. Continued irradiation causes further nucleation and growth of droplets. While early stage growth is dominated by diffusion and dynamic coarsening, there is a transition to late-stage growth dominated by Ostwald ripening and dynamic coalescence. The foregoing arguments appear to indicate that the (modified) Bradley–Harper models outlined in the previous section cannot readily explain the formation of the highly periodic nanodot arrays observed in these studies [148,149].

In other experiments using FIB systems for irradiation [150–155], extended wall-like structures were found to develop at the periphery of the bombarded areas upon Ga implantation. The AFM topography image in Fig. 16a shows such wall-like features at the boundary region of an irradiated area for a Ge specimen bombarded by 30 keV Ga^+ ions with $3 \times 10^{16} \text{ ions/cm}^2$ [155]. Figure 16b displays a cross-section line profile of that area and illustrates the pertinent features. For Si and Ge specimens, the height of this wall was found to increase with increasing fluence, reaching a value of $\sim 15 \text{ nm}$ at $1 \times 10^{17} \text{ Ga}^+\text{-ions/cm}^2$ [155].

Similar structures were observed in a study using a Fe/Cr/Fe multilayer system, bombarded by 30 keV Ga^+ ions in an FIB instrument [156]. In this specimen, four pinnacle-like elevations were found in addition at the corners of the region hit by the ions. The height of these “pinnacles” (of about 25 nm) exceeds significantly the one in the center of the sidewalls (of about 10 nm). Both the sidewalls and the pinnacles are characterized by an almost triangular profile with a smoothed-out top. The full width at half-maximum (FWHM) is of about 250 and 150 nm for the pinnacles and the sidewalls, respectively. The wall-like elevations appearing at the periphery of the irradiated areas were experimentally analyzed by varying the irradiation conditions [156]. The results demonstrated that the wall size (height/width) is approximately inversely proportional to the ion current density applied. An analysis of these experimental results together with corresponding estimations (based partially on literature data) lead the authors [156] to interpret this topographic feature as an ensemble of coalesced adatoms (adatom clus-

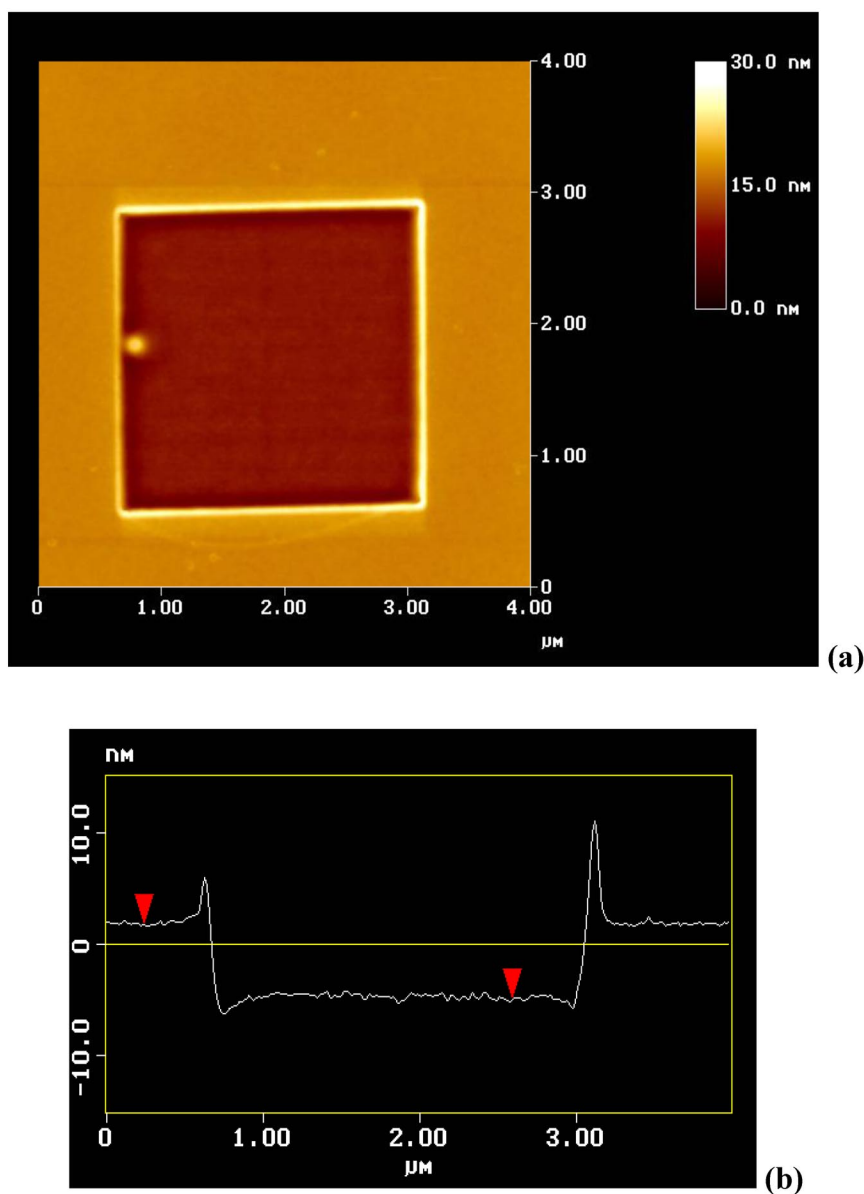


Fig. 16 (a) AFM topography image of a Ge surface area ($2.5 \times 2.5 \mu\text{m}$) irradiated with 30 keV Ga^+ ions at a fluence of $3 \times 10^{16} \text{ cm}^{-2}$. (b) Line scan across the image in (a), showing the wall structure at the periphery of the bombarded region. From [155].

ters), produced by ion bombardment, with temperature effects during ion irradiation playing a decisive role.

CONCLUSIONS

Ion bombardment of surfaces is intrinsically a stochastic process, as can be seen from the images of single-ion impact events shown in the second section. Notwithstanding, prolonged ion irradiation may lead

to highly regular surface patterns, with nm-sized dimensions. Many experiments and simulations appear to indicate that these structures result basically from a balance between effects that tend to cause a roughening of the surface (such as sputtering) and those that lead to surface smoothing via, e.g., diffusion or other transport processes. Still, many aspects of those mechanisms and their interplay are not fully understood presently. Given the sound progress made during the past decade, one may anticipate, however, that future studies will improve this situation and could make ion-induced surface nano-patterning a standard tool in materials science. In fact, the high regularity of such structures and their small dimensions make them attractive candidates for many applications, some of which are in a stage of exploration [88,157–160].

ACKNOWLEDGMENTS

I am grateful to Frank Frost, Thomas Michely, and Herbert Urbassek for granting the permission to reproduce some of their published results. Financial support from the Deutsche Forschungsgemeinschaft under grant GN 18/25-1 is acknowledged.

REFERENCES

1. M. Kaminsky. *Atomic and Ionic Impact Phenomena on Metal Surfaces*, Springer, Berlin (1965).
2. G. Leibfried. *Bestrahlungseffekte in Festkörpern*, Teubner, Stuttgart (1965).
3. G. Carter, J. S. Colligon. *Ion Bombardment of Solids*, Heineman, London (1968).
4. Ch. Lehmann. *Interaction of Radiation with Solids and Elementary Defect Production*, North-Holland, Amsterdam (1977).
5. G. Carter, B. Navinšek, J. L. Whitton. In: *Sputtering by Particle Bombardment II*, R. Behrisch (Ed.), p. 231, Springer, Berlin (1983).
6. O. Auciello, R. Kelly (Eds.). *Ion Beam Modifications of Surfaces*, Elsevier, Amsterdam (1984).
7. J. W. Rabalais (Ed.). *Low Energy Ion-Surface Interactions*, John Wiley, Chichester (1994).
8. M. Nastasi, J. W. Mayer, J. K. Hirvonen. *Ion Solid Interactions: Fundamentals and Applications*, Cambridge University Press, Cambridge (1996).
9. H. Gnaser. *Low-Energy on Irradiation of Solid Surfaces*, Springer, Berlin (1999).
10. P. Sigmund. *Particle Penetration and Radiation Effects*, Springer, Berlin (2006).
11. G. Carter. *J. Phys. D: Appl. Phys.* **34**, R1 (2001).
12. M. A. Makeev, R. Cuerno, A.-L. Barabási. *Nucl. Instrum. Methods B* **197**, 185 (2002).
13. U. Valbusa, C. Boragno, F. Buatier de Mongeot. *J. Phys.: Condens. Matter* **14**, 8153 (2002).
14. W. L. Chan, E. Chason. *J. Appl. Phys.* **101**, 121301 (2007).
15. R. P. Webb, D. E. Harrison. *Phys. Rev. Lett.* **50**, 1478 (1983).
16. D. E. Harrison, R. P. Webb. *Nucl. Instrum. Methods* **218**, 727 (1983).
17. (a) D. E. Harrison. *Radiat. Eff. Defects Solids* **70**, 1 (1983); (b) D. E. Harrison. *Crit. Rev. Solid State Mater. Sci.* **14**, S1 (1988).
18. F. Karetta, H. M. Urbassek. *J. Appl. Phys.* **71**, 5410 (1992).
19. H. Gades, H. M. Urbassek. *Phys. Rev. B* **50**, 11167 (1994).
20. M. Ghaly, K. Nordlund, R. S. Averback. *Philos. Mag. A* **79**, 795 (1999).
21. T. J. Colla, H. M. Urbassek. *Phys. Rev. B* **62**, 8487 (2000).
22. N. J. Zheng, I. H. Wilson, U. Knipping, D. M. Burt, D. H. Krinsley, I. S. T. Tsong. *Phys. Rev. B* **38**, 12780 (1988).
23. (a) I. H. Wilson, N. J. Zheng, U. Knipping, I. S. T. Tsong. *Phys. Rev. B* **38**, 8444 (1988); (b) I. H. Wilson, N. J. Zheng, U. Knipping, I. S. T. Tsong. *Appl. Phys. Lett.* **53**, 2039 (1988).
24. C. A. Lang, C. F. Quate, J. Nogami. *Appl. Phys. Lett.* **59**, 1696 (1991).
25. J. C. Girard, Y. Samson, S. Gauthier, S. Rousset, J. Klein. *Surf. Sci.* **302**, 73 (1994).
26. J. R. Hahn, H. Kang. *Surf. Sci.* **357/358**, 165 (1996).

27. J. Naumann, J. Osing, A. J. Quinn, I. V. Shvets. *Surf. Sci.* **388**, 212 (1997).
28. T. Michely, G. Comsa. *Phys. Rev. B* **44**, 8411 (1991).
29. T. Michely, T. Land, U. Littmark, G. Comsa. *Surf. Sci.* **272**, 204 (1992).
30. T. Michely, C. Teichert. *Phys. Rev. B* **50**, 11156 (1994).
31. M. Morgenstern, T. Michely, G. Comsa. *Philos. Mag. A* **79**, 775 (1999).
32. A. Redinger, S. Standop, T. Michely, Y. Rosandi, H. M. Urbassek. *Phys. Rev. Lett.* **104**, 075501 (2010).
33. H. J. W. Zandvliet, H. B. Elswijk, E. J. van Loenen, I. S. T. Tsong. *Phys. Rev. B* **46**, 7581 (1992).
34. H. Feil, H. J. W. Zandvliet, M.-H. Tsai, J. D. Dow, I. S. T. Tsong. *Phys. Rev. Lett.* **69**, 3076 (1992).
35. N. Kitamura, M. G. Lagally, M. B. Webb. *Phys. Rev. Lett.* **71**, 2082 (1993).
36. S. J. Chey, J. E. van Nostrand, D. G. Cahill. *Phys. Rev. B* **52**, 16696 (1995).
37. S. J. Chey, D. G. Cahill. *Surf. Sci.* **380**, 377 (1997).
38. T. Seki, T. Aoki, J. Matsuo, I. Yamada. *Nucl. Instrum. Methods B* **164–165**, 650 (2000).
39. J. A. Floro, B. K. Kellerman, E. Chason, S. T. Picraux, D. K. Brice, K. M. Horn. *J. Appl. Phys.* **77**, 2351 (1995).
40. X.-S. Wang, R. J. Pechman, J. H. Weaver. *J. Vac. Sci. Technol. B* **13**, 2031 (1995).
41. R. J. Pechman, X.-S. Wang, J. H. Weaver. *Phys. Rev. B* **51**, 10929 (1995).
42. X.-S. Wang, R. J. Pechman, J. H. Weaver. *Surf. Sci.* **364**, L511 (1996).
43. A.-L. Barabási, H. E. Stanley. *Fractal Concepts in Surface Growth*, Cambridge University Press, Cambridge (1995).
44. F. Family, T. Vicsek. *J. Phys. A: Math. Gen.* **18**, L75 (1985).
45. F. Family. *J. Phys. A: Math. Gen.* **19**, L441 (1986).
46. P. Meakin. *Phys. Rep.* **235**, 189 (1993).
47. J. Lapujoulade. *Surf. Sci. Rep.* **20**, 191 (1994).
48. T. Michely, G. Comsa. *Nucl. Instrum. Methods B* **82**, 207 (1993).
49. T. Michely, M. Kalff, G. Comsa, M. Strobel, K.-H. Heinig. *Phys. Rev. Lett.* **86**, 2589 (2001).
50. M. Kalff, G. Comsa, T. Michely. *Surf. Sci.* **486**, 103 (2001).
51. H. Hansen, C. Polop, T. Michely, A. Friedrich, H. M. Urbassek. *Phys. Rev. Lett.* **92**, 246106 (2004).
52. H. Hansen, A. Redinger, S. Messlinger, G. Stoian, Y. Rosandi, H. M. Urbassek, U. Linke, T. Michely. *Phys. Rev. B* **73**, 235414 (2006).
53. A. Redinger, H. Hansen, U. Linke, Y. Rosandi, H. M. Urbassek, T. Michely. *Phys. Rev. Lett.* **96**, 106103 (2006).
54. R. L. Cunningham, P. Haymann, C. Lecomte, W. J. Moore, J. J. Trillat. *J. Appl. Phys.* **31**, 839 (1960).
55. M. Navez, C. Sella, D. Chaperot. *C. R. Acad. Sci. (Paris)* **254**, 240 (1962).
56. S. Habenicht, W. Bolse, K. P. Lieb, K. Reimann, U. Geyer. *Phys. Rev. B* **60**, R2200 (1999).
57. S. Habenicht. *Phys. Rev. B* **63**, 125419 (2001).
58. S. Rusponi, C. Boragno, U. Valbusa. *Phys. Rev. Lett.* **78**, 2795 (1997).
59. S. Rusponi, G. Constantini, C. Boragno, U. Valbusa. *Phys. Rev. Lett.* **81**, 2735 (1998).
60. S. Rusponi, G. Constantini, C. Boragno, U. Valbusa. *Phys. Rev. Lett.* **81**, 4184 (1998).
61. R. Moroni, D. Sekiba, F. Buatier de Mongeot, G. Gonella, C. Boragno, L. Mattera, U. Valbusa. *Phys. Rev. Lett.* **91**, 167207 (2003).
62. P. Karmakar, D. Ghose. *Surf. Sci.* **554**, L101 (2004).
63. M. O. Liedke, B. Liedke, A. Keller, B. Hillebrands, A. Mücklich, S. Facsko, J. Fassbender. *Phys. Rev. B* **75**, 220407 (2007).
64. K. Zhang, F. Rotter, M. Uhrmacher, C. Ronning, J. Krauser, H. Hofsäss. *New J. Phys.* **9**, 29 (2007).
65. H. Hofsäss, K. Zhang. *Appl. Phys. A* **92**, 517 (2008).
66. P. Mishra, D. Ghose. *J. Appl. Phys.* **104**, 094305 (2008).

67. D. Ghose. *J. Phys.: Condens. Matter* **21**, 224001 (2009).
68. P. Mishra, D. Ghose. *J. Appl. Phys.* **105**, 014304 (2009).
69. F. A. Stevie, P. M. Kahora, D. S. Simons, P. Chi. *J. Vac. Sci. Technol. A* **6**, 76 (1988).
70. A. Karen, K. Okuno, F. Soeda, A. Ishitani. *J. Vac. Sci. Technol. A* **9**, 2247 (1991).
71. S. W. MacLaren, J. E. Baker, N. L. Finnegan, C. M. Loxton. *J. Vac. Sci. Technol. A* **10**, 468 (1992).
72. Z. X. Jiang, P. F. A. Alkemade. *Appl. Phys. Lett.* **73**, 315 (1998).
73. S. Facsko, T. Dekorsy, C. Koerdts, C. Trappe, H. Kurz, A. Vogt, H. L. Hartnagel. *Science* **285**, 1551 (1999).
74. S. Facsko, T. Bobek, T. Dekorsy, H. Kurz. *Phys. Status Solidi B* **224**, 537 (2001).
75. J. Kim, D. G. Cahill, R. S. Averback. *Phys. Rev. B* **67**, 045404 (2003).
76. F. Frost, B. Rauschenbach. *Appl. Phys. A* **77**, 1 (2003).
77. B. Ziberi, F. Frost, B. Rauschenbach, T. Höche. *Appl. Phys. Lett.* **87**, 033113 (2005).
78. B. Ziberi, F. Frost, B. Rauschenbach. *Appl. Phys. Lett.* **88**, 173115 (2006).
79. Y. Wang, S. F. Yoon, C. Y. Ngo, J. Ahn. *Nanoscale Res. Lett.* **2**, 504 (2007).
80. B. Ziberi, F. Frost, M. Tartz, H. Neumann, B. Rauschenbach. *Appl. Phys. Lett.* **92**, 063102 (2008).
81. F. Frost, B. Ziberi, A. Schindler, B. Rauschenbach. *Appl. Phys. A* **91**, 551 (2008).
82. B. Ziberi, M. Cornejo, F. Frost, B. Rauschenbach. *J. Phys.: Condens. Matter* **21**, 224003 (2009).
83. T. K. Chini, D. P. Datta, S. R. Bhattacharyya. *J. Phys.: Condens. Matter* **21**, 224004 (2009).
84. I. S. Nerbø, S. Le Roy, M. Kildemo, E. Søndergård. *Appl. Phys. Lett.* **94**, 213105 (2009).
85. S. Le Roy, E. Barthel, N. Brun, A. Lelarge, E. Søndergård. *J. Appl. Phys.* **106**, 094308 (2009).
86. N. G. Shang, F. Y. Meng, F. C. K. Au, Q. Li, C. S. Lee, I. Bello, S. T. Lee. *Adv. Mater.* **14**, 1308 (2002).
87. G. Ozaydin, A. S. Özcan, Y. Wang, K. F. Ludwig, D. P. Siddons. *Appl. Phys. Lett.* **87**, 163104 (2005).
88. C. Teichert, C. Hofer, G. Hlawacek. *Adv. Eng. Mater.* **8**, 1057 (2006).
89. J. A. Sánchez-García, L. Vázquez, R. Gago, A. Redondo-Cubero, J. M. Albella, Zs. Czigány. *Nanotechnology* **19**, 355306 (2008).
90. J. A. Sánchez-García, R. Gago, R. Caillard, A. Redondo-Cubero, J. A. Martín-Gago, F. J. Palomares, M. Fernández, L. Vázquez. *J. Phys.: Condens. Matter* **21**, 224009 (2009).
91. G. Ozaydin-Ince, K. F. Ludwig. *J. Phys.: Condens. Matter* **21**, 224008 (2009).
92. J. Zhou, M. Lu. *Phys. Rev. B* **82**, 125404 (2010).
93. S. Macko, F. Frost, B. Ziberi, D. F. Förster, T. Michely. *Nanotechnology* **21**, 085301 (2010).
94. K. Zhang, M. Brötzmann, H. Hofsäss. *New J. Phys.* **13**, 013033 (2011).
95. M. Cornejo, B. Ziberi, C. Meinecke, D. Hirsch, J. W. Gerlach, T. Höche, F. Frost, B. Rauschenbach. *Appl. Phys. A* **102**, 593 (2011).
96. J. Erlebacher, M. J. Aziz, E. Chason, M. B. Sinclair, J. A. Floro. *Phys. Rev. Lett.* **82**, 2330 (1999).
97. A. Datta, Y.-R. Wu, Y. L. Wang. *Phys. Rev. B* **63**, 125407 (2001).
98. T. K. Chini, M. K. Sanyal, S. R. Bhattacharyya. *Phys. Rev. B* **66**, 153404 (2002).
99. A.-D. Brown, J. Erlebacher, W.-L. Chan, E. Chason. *Phys. Rev. Lett.* **95**, 056101 (2005).
100. S. Ichim, M. J. Aziz. *J. Vac. Sci. Technol. B* **23**, 1068 (2005).
101. B. Ziberi, F. Frost, B. Rauschenbach. *Appl. Phys. Lett.* **88**, 173115 (2006).
102. H. Zhou, Y. Wang, L. Zhou, R. L. Headrick, A. S. Özcan, Y. Wang, G. Özaydin, K. F. Ludwig, D. P. Siddons. *Phys. Rev. B* **75**, 155416 (2007).
103. V. B. Shenoy, W. L. Chan, E. Chason. *Phys. Rev. Lett.* **98**, 256101 (2007).
104. A. Keller, S. Facsko, W. Möller. *New J. Phys.* **10**, 063004 (2008).
105. A. Keller, R. Cuerno, S. Facsko, W. Möller. *Phys. Rev. B* **79**, 115437 (2009).
106. F. Krok, S. R. Saeed, Z. Postawa, M. Szymonski. *Phys. Rev. B* **79**, 235432 (2009).
107. S. Habenicht, K. P. Lieb, J. Koch, A. D. Wieck. *Phys. Rev. B* **65**, 115327 (2002).
108. P. F. A. Alkemade. *Phys. Rev. Lett.* **96**, 107602 (2006).

109. Q. Wei, J. Lian, L. A. Boatner, L. M. Wang, R. C. Ewing. *Phys. Rev. B* **80**, 085113 (2009).
110. B. Reuscher, H. Gnaser. To be published.
111. R. M. Bradley, J. M. E. Harper. *J. Vac. Sci. Technol. A* **6**, 2390 (1988).
112. R. Cuerno, A.-L. Barabási. *Phys. Rev. Lett.* **74**, 4746 (1995).
113. M. Kardar, G. Parisi, Y.-C. Zhang. *Phys. Rev. Lett.* **56**, 889 (1986).
114. M. Castro, R. Cuerno, L. Vázquez, R. Gago. *Phys. Rev. Lett.* **94**, 016102 (2005).
115. S. Vogel, S. Linz. *Phys. Rev. B* **75**, 085425 (2007).
116. Y. Kuramoto, T. Tsuzuki. *Prog. Theor. Phys.* **55**, 356 (1977).
117. G. I. Sivashinsky. *Acta Astron.* **6**, 569 (1979).
118. M. Rost, J. Krug. *Phys. Rev. Lett.* **75**, 3894 (1995).
119. M. A. Makeev, A.-L. Barabási. *Appl. Phys. Lett.* **71**, 2800 (1997).
120. S. Facsko, T. Bobek, A. Stahl, H. Kurz, T. Dekorsy. *Phys. Rev. B* **69**, 153412 (2004).
121. P. Sigmund. *J. Mater. Sci.* **8**, 1545 (1973).
122. E. Chason, T. M. Mayer, B. K. Kellerman, D. N. McIlroy, A. J. Howard. *Phys. Rev. Lett.* **72**, 3040 (1994).
123. T. M. Mayer, E. Chason, A. J. Howard. *J. Appl. Phys.* **76**, 1633 (1994).
124. M. J. Aziz. *K. Dan. Vidensk. Selsk. Mat. Fys. Medd.* **52**, 187 (2006).
125. R. M. Bradley. *Phys. Rev. E* **54**, 6149 (1996).
126. G. Carter, V. Vishnyakov. *Phys. Rev. B* **54**, 17647 (1996).
127. M. Moseler, P. Gumbsch, C. Casiraghi, A. C. Ferrari, J. Robertson. *Science* **309**, 1545 (2005).
128. B. Davidovitch, M. J. Aziz, M. P. Brenner. *Phys. Rev. B* **76**, 205420 (2007).
129. S. A. Norris, M. P. Brenner, M. J. Aziz. *J. Phys.: Condens. Matter* **21**, 224020 (2009).
130. C. S. Madi, E. Anzenberg, K. F. Ludwig, M. J. Aziz. *Phys. Rev. Lett.* **106**, 066101 (2011).
131. J. Muñoz-García, M. Castro, R. Cuerno. *Phys. Rev. Lett.* **96**, 086101 (2006).
132. J. Muñoz-García, R. Cuerno, M. Castro. *Phys. Rev. B* **78**, 205408 (2008).
133. J. Muñoz-García, R. Cuerno, M. Castro. *J. Phys.: Condens. Matter* **21**, 224017 (2009).
134. R. M. Bradley, P. D. Shipman. *Phys. Rev. Lett.* **105**, 145501 (2010).
135. J. Orloff, M. Utlaut, L. Swanson. *High Resolution Focused Ion Beams: FIB and its Applications*, Kluwer Academic, New York (2003).
136. L. A. Giannuzzi, F. A. Stevie (Eds.). *Introduction to Focused Ion Beams: Theory, Techniques, and Practice*, Springer, Berlin (2005).
137. A. A. Tseng. *Small* **1**, 924 (2005).
138. C. A. Volkert, A. M. Minor. *MRS Bull.* **32**, 389 (2007).
139. R. L. Kubena, J. W. Ward, F. P. Stratton, R. J. Joyce, G. M. Atkinson. *J. Vac. Sci. Technol. B* **9**, 3079 (1991).
140. J. Orloff. *Rev. Sci. Instrum.* **64**, 1105 (1993).
141. H. H. Chen, O. A. Urquidez, S. Ichim, L. H. Rodriguez, M. P. Brenner, M. J. Aziz. *Science* **310**, 294 (2005).
142. D. P. Adams, T. M. Mayer, M. J. Vasile, K. Archuleta. *Appl. Surf. Sci.* **252**, 2432 (2006).
143. K. Zhao, R. S. Averback, D. G. Cahill. *Appl. Phys. Lett.* **89**, 053103 (2006).
144. J. Lian, L. Wang, X. Sun, Q. Yu, R. C. Ewing. *Nano Lett.* **6**, 1047 (2006).
145. Q. Wei, W. Li, K. Sun, J. Lian, L. Wang. *J. Appl. Phys.* **103**, 074306 (2008).
146. Q. Wei, X. Zhou, B. Joshi, Y. Chen, K.-D. Li, Q. Wie, K. Sun, L. Wang. *Adv. Mater.* **21**, 2865 (2009).
147. W. J. MoberlyChan. *J. Phys.: Condens. Matter* **21**, 224013 (2009).
148. Q. Wei, J. Lian, W. Lu, L. Wang. *Phys. Rev. Lett.* **100**, 076103 (2008).
149. J. H. Wu, W. Ye, B. L. Cardozo, D. Saltzman, K. Sun, H. Sun, J. F. Mansfield, R. S. Goldman. *Appl. Phys. Lett.* **95**, 153107 (2009).
150. L. Bischoff, J. Teichert, V. Heera. *Appl. Surf. Sci.* **184**, 372 (2001).
151. A. Lugstein, B. Basnar, J. Smoliner, E. Bertagnolli. *Appl. Phys. A* **76**, 545 (2003).

152. B. D. Huey, R. M. Langford. *Nanotechnology* **14**, 409 (2003).
153. G. C. Gazzadi, P. Luches, S. F. Contri, A. di Bona, S. Valeri. *Nucl. Instrum. Methods B* **230**, 512 (2005).
154. S. Blomeier, B. Hillebrands, V. E. Demidov, S. O. Demokritov, B. Reuscher, A. Brodyanski, M. Kopnarski. *J. Appl. Phys.* **98**, 093503 (2005).
155. H. Gnaser, A. Brodyanski, B. Reuscher. *Surf. Interf. Anal.* **40**, 1415 (2008).
156. A. Brodyanski, S. Blomeier, W. Bock, H. Gnaser, B. Hillebrands, M. Kopnarski, B. Reuscher. To be published.
157. T. W. H. Oates, A. Keller, S. Noda, S. Facsko. *Appl. Phys. Lett.* **93**, 063106 (2008).
158. J. Fassbender, T. Strache, M. O. Liedke, D. Markó, S. Wintz, K. Lenz, A. Keller, S. Facsko, I. Mönch, J. McCord. *New J. Phys.* **11**, 125002 (2009).
159. F. Buatier de Mongeot, U. Valbusa. *J. Phys.: Condens. Matter* **21**, 224022 (2009).
160. C. Teichert, J. J. de Miguel, T. Bobek. *J. Phys.: Condens. Matter* **21**, 224025 (2009).